

A Measurement of The Faint Source Correlation Function in the GOODS and UDF Surveys

Eric Morganson¹ and Roger Blandford¹

¹KIPAC, P.O. Box 20450, MS29, Stanford, CA 94309, USA

Accepted —; received —; in original form 30 October 2018

ABSTRACT

We present a stable procedure for defining and measuring the two point angular autocorrelation function, $w(\theta) = (\theta/\theta_0(V))^{-\Gamma}$, of faint ($25 < V < 29$), barely resolved and unresolved sources in the HST GOODS and UDF datasets. We construct catalogs that include close pairs and faint detections. We show, for the first time, that, on subarcsecond scales, the correlation function exceeds unity. This correlation function is well fit by a power law with index $\Gamma \approx 2.5$ and a $\theta_0 = 10^{-0.1(V-25.8)}$ arcsec. This is very different from the values of $\Gamma \approx 0.7$ and $\theta_0(r) = 10^{-0.4(r-21.5)}$ arcsec associated with the gravitational clustering of brighter galaxies. This observed clustering probably reflects the presence of giant star-forming regions within galactic-scale potential wells. Its measurement enables a new approach to measuring the redshift distribution of the faintest sources in the sky.

Key words: galaxies: distances and redshifts - galaxies: evolution - galaxies: statistics - galaxies: structure

1 INTRODUCTION

The two-point angular and spatial autocorrelation functions, $w(\theta)$ and $\xi(r)$ are defined as:

$$\left\langle \frac{dP}{d\vec{\theta}}(\vec{\theta}_0) \frac{dP}{d\vec{\theta}}(\vec{\theta}_0 + \vec{\theta}) \right\rangle = \sigma_0^2(1 + w(\theta)) \quad (1)$$

and

$$\left\langle \frac{dP}{d\vec{r}}(\vec{r}_0) \frac{dP}{d\vec{r}}(\vec{r}_0 + \vec{r}) \right\rangle = \rho_0^2(1 + \xi(r)) \quad (2)$$

The correlation function of galaxies has been studied observationally at least as far back as Totsuji & Kihara (1969). Most recently, the large scale angular correlation function, $w(\theta)$, function was measured for the galaxies in the Sloan Digital Sky Survey (SDSS) (Connolly et al. 2002) for sources with magnitude $18 < r < 22$ and on scales $10'' < \theta < 1000''$. This and similar work with the 2 Degree Galaxy Redshift Survey (2DF) (Hawkins et al. 2003) confirmed that $w(\theta)$ is consistent with a power law form (see Fig. 1):

$$w(\theta, r) = \left(\frac{\theta}{\theta_0(r)} \right)^{-\Gamma} \quad (3)$$

where:

$$\theta_0(r) = 10^{-0.4(r-21.5)} \text{ arcsec}; \Gamma = 0.72 \quad (4)$$

θ_0 is roughly proportional to the flux of the source. If we were to extrapolate this trend out to $r < 25$, we would expect a $\theta_0 = 0.054''$, too small to observe with current data.

Both the SDSS and 2DF groups measured the spatial correlation function (Zehavi et al. 2002) (Hawkins et al. 2003). SDSS ob-

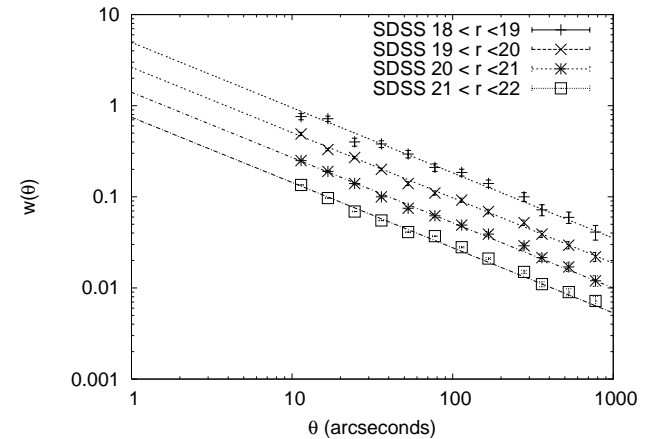


Figure 1. The SDSS correlation function with different limiting magnitudes.

served $r < 22.5$, $0.02 < z < 0.13$ sources on scales of $0.14 \text{ Mpc} < r < 23 \text{ Mpc}$. These observations essentially confirm a power law model of the correlation function with exponent $\gamma \approx \Gamma + 1$, consistent with Limber (1953):

$$\xi(r) = \left(\frac{r}{r_0} \right)^{-\gamma}; r_0 \approx r_c \theta_0^{\Gamma/(\Gamma+1)} \quad (5)$$

where r_c is the characteristic distance to the sources and the sources are distributed with a width $\Delta r_c \approx r_c$.

Masjedi et al. (2006) extended the SDSS measurement of $\xi(r)$ down to 14 kpc with moderate resolution difficulties on the smallest scales and found that $\xi(r)$ is consistent with a $\Gamma = 2$ power law over four orders of magnitude.

Peebles (1974) proposed that the cosmological scale correlation function and its power spectrum counterpart should be related to the microwave background fluctuation using the theory of gravitational perturbations. On cosmological scales, the dark matter correlation function evolved from primordial mass fluctuations. Halo Occupation Distribution (HOD) frameworks are used to predict galaxy bias within large dark matter halos (Peacock & Smith 2000). Today, theory and experiment are in excellent agreement on the largest scales e.g. Tegmark et al. (2004), and measurements down to 0.3 Mpc, including slight perturbations from a power law, can be explained in the HOD framework (Zehavi et al. 2004). The continuation of a power law down to smaller scales is less understood, but Masjedi et al. (2006) note that it could be accommodated by HOD models with reasonable modifications.

Measurements of $\xi(r)$ are fundamentally restricted to bright sources by the need for redshifts. HST and large telescopes make spectroscopic redshift measurements good for $r < 25$ and photometric measurements for $r < 27$ (Coe et al. 2006). But the faintest photometric redshifts cannot be calibrated. Ellipticity measurements are very uncertain for sources which are not significantly larger than the PSF, which hinders HST ellipticity measurements for sources dimmer than $r \approx 26$. But even for the faintest sources, we can precisely measure position and, with a large enough sample, $w(\theta)$.

The $25 < V < 29$ sources we study in the paper are only $0.1'' - 0.5''$ in size, no more than a few kpc across at any redshift and much smaller than local galaxies. We find that these sources are only significantly clustered on subarcsecond scales. Even at high redshifts, the physical correlation scales would be roughly 5 kpc and smaller, much smaller than the scales probed by Masjedi et al. (2006). These sources tend to be bluer than the luminous red galaxies (LRG)s selected by the SDSS groups, as they were selected in the V band. Blue sources with sub-galactic luminosities and sizes separated by sub-galactic distances are likely to be separate star-forming regions in the same dark matter potential wells. The cosmological effect which causes the correlation function observed in SDSS might have some influence at such small scales, but effects other than gravity - gas dynamics, star formation, supernovae and so on - dominate over any simple halo modeling. In addition, the faint source correlation function (FSCF) traces luminosity, but its relationship to mass is unclear.

Measuring $w(\theta)$ for faint sources on small scales is an important method of probing how these primarily non-gravitational effects augment the gravitational correlation function. With much larger datasets, we could study the transition from gravitational to non-gravitational domination in the correlation function. Despite the fact that this is not possible with current data, the FSCF is interesting in its own right as a useful time-dependent tracer of star formation and galactic structure,

The small, faint sources we study are an important astrophysical mystery. If we extrapolate the source counts from the Hubble Ultra Deep Field (UDF) to the whole sky, we estimate that there are $\approx 10^{11}$ sources in the sky, and yet if we extend our local galaxy density out to the $\approx 10^{12}$ Mpc³ comoving volume within $z \leq 4$, we obtain roughly one tenth this number. These sources are therefore likely to be the subunits of future galaxies and studying their redshift distribution would be a useful way to probe galaxy assembly. Unfortunately, we do not know the distance to these sources.

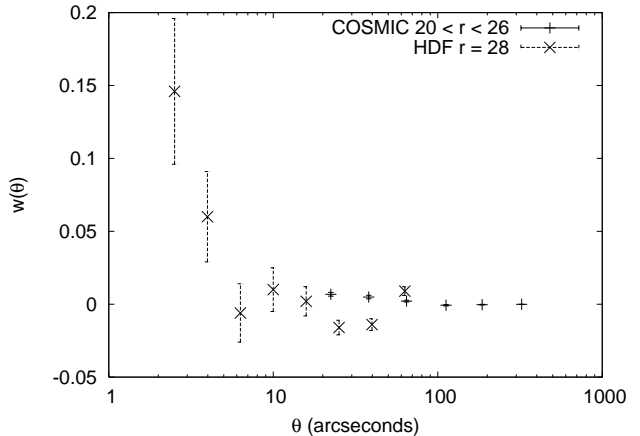


Figure 2. The faint correlation function in COSMIC (Brainerd et al. 1995) and the HDF (Villumsen et al. 1997).

Previous estimates have ranged from $z < 1$ (Babul & Rees 1992) to $z \approx 2.5$ (He et al. 2000). Their dimness and small size make them difficult to study photometrically or geometrically, but we can study the way they cluster with some precision.

In this paper, we observe the FSCF in the HST GOODS and UDF in the $0.3'' < \theta < 10''$ range. The excellent angular resolution allows us to make the first statistically significant measurement of the $w(\theta)$ for faint sources and to measure both θ_0 and Γ . In SDSS, Li et al. (2007) found a significant correlation function of $r < 17.8$ sources on scales down to 10 kpc $\approx 2''$ at their limiting redshift of $z = 0.3$. Brainerd et al. (1995) studied the correlation function of $r < 26$ sources down to scales of $30''$ using the COSMIC imaging spectrograph and showed that they were on the order of 0.01 at these large scales. Villumsen et al. (1997) used $r < 29$ sources on scales down to $3''$ in the Hubble Deep Field (HDF) but did not find a correlation function larger than 0.2 or more than 2σ greater than 0. Connolly et al. (1998) used the $i < 27$ sources to confirm that $w(\theta)$ was on the scale of 0.1 for arcsecond $\theta \approx 1''$. As shown in Fig. 2, the groups studying faint sources found $w(\theta)$ was equal to only a few tenths and barely statistically significant.

In section 2 of this paper, we discuss the data used to make these measurements. In section 3, we explain our computational methods for producing simulated images. In section 4, we describe the production and characteristics of catalogs used in this analysis. We discuss how we produce our estimate of the correlation function in section 5. In section 6, we present our best fit models to the data, and in section 7 we discuss the astrophysical significance of our findings and how they could be applied to future surveys.

In future papers, we will show that the three-point autocorrelation function is also measurable for these faint sources. We will provide a formalism to measure how the two-point correlation function is distorted by a gravitational lens and use it to relate the distributions of source and lens redshifts to the extent permitted by existing data. Finally, we will measure this effect and use it to relate the distributions of source and lens redshifts to the extent permitted by existing data.

2 SAMPLES

Previous measurements of the FSCF were limited by low resolution and poor statistics. To overcome resolution difficulties, we use HST observations with roughly $0.12''$ resolution. To improve upon HDF

	F435W	F606W	F775W	F850LP
GOODS	27.8	27.8	27.1	26.6
UDF	29.1	29.3	29.2	28.7

Table 1. The limiting magnitudes for 10σ detections of point sources in different bands of GOODS and UDF.

measurements we use samples which are either larger or deeper to increase the number of total sources. We measure the positions of the $25 < V < 28$ sources in the HST Great Observatories Origins Deep Survey (GOODS) North and South (Giavalisco et al. 2004) and make $27 < V < 29$ measurements in the HST UDF (Beckwith et al. 2006).

The GOODS fields cover roughly 160 arcmin^2 each in the ACS *BVi*z bands (F435W, F606W, F814W, and F850LP). The *V* band limiting magnitude for a 10σ detection of a point source is 27.8. The standard catalogs made detections in the *z* band and found 29599 sources in the South and 32048 sources in the North. Using methods detailed in section 4, we produce catalogs with 56088 and 60182 sources in the South and North respectively.

The UDF covers roughly 11 arcmin^2 in the same bands but probes roughly 1.5 m deeper than GOODS. The *V* band limiting magnitude for a 10σ detection of a point source is 29.3. A standard catalog was made in the *i* band with 10,040 sources. Using methods described in section 4, we produce *V* band catalogs with 7298 sources.

Studying the angular correlation in HST Cosmic Evolution Survey (COSMOS) would be an interesting extension to this work. COSMOS covers two square degrees and is complete for $0.5''$ sources down to $i = 26$ (Scoville et al. 2007). This is roughly equivalent to a $V = 25$ for typical sources. Measuring the FSCF in COSMOS would allow us to fill in the gap between the $V > 25$ work here and the $r < 22$ work in SDSS. Unfortunately, the enormous size of COSMOS make the simulation techniques we use here impractical, and measuring the COSMOS correlation function will have to be a separate effort.

3 PRODUCING SIMULATED DATA

In order to measure the FSCF accurately, we must correct for non-astronomical correlation effects like optical resolution limits, the incorrect deblending of sources of non-zero size and the clustering of noise peaks. Simulated images are our main tool in estimating these effects and determining how to make the best catalogs for these observations.

To make simulated data, we generated images with only sources, convolved them with a simulated HST ACS PSF and added Gaussian noise fields that had been convolved with a separate noise correlation PSF. We tested and rejected many parameterizations of the source characteristics, source distribution, noise models and PSFs. This simulation required that many parameters be fine-tuned to match the statistical properties of GOODS and UDF. In the following descriptions we describe these parameters, the values we adopted and the quantitative rationale for these choices.

3.1 Simulated Source Profiles

We compared real ($25 < V < 27$) sources to the best fit de Vaucouleurs, Lorentzian, exponential and Gaussian profiles. After considerable experimentation, we adopted the de Vaucouleurs profile, but found that it performed only moderately better than the other

profiles, because the sources are small and barely above threshold. For all fits, the profile is assumed to be elliptical, and we convert to fit to a circular profile using an effective radius, r defined by:

$$r^2 = a_1(x - x_0)^2 + a_2(y - y_0)^2 + a_3(x - x_0)(y - y_0) \quad (6)$$

with (x_0, y_0) being fit to define a centre and (a_1, a_2, a_3) being fit to give the source an arbitrary ellipticity and orientation.

In the case of the de Vaucouleurs profile, we taper the sharp central peak when $r^2 < 0.5r_{1/2}^2$ where $r_{1/2}$ is the half light radius. In this central region of a few pixels, we replace r^2 with $0.25(r_{1/2}^2 + r^2)$. The sharp peak would be flattened by the PSF and is in fact not even observed in fully resolved sources (Alam & Ryden 2002).

In addition to the above shape parameters, we also fit an integral intensity, I_C , and a simple background with a linearly varying intensity so that the function to which we fit surface brightness:

$$B(x, y) = b_0 + b_1x + b_2y + I_0I(r^2) \quad (7)$$

where I is the normalized intensity of the profile being tested.

For each source the data is fit inside of a square with sides of length $3\sqrt{A}$ where A is the detection area (a typical source and fit is in Fig. 3). We use the standard deviations implied by the weight images and compare the χ^2 over degrees of freedom for each fit type. We find that our modified de Vaucouleurs profile has an average χ^2/N_{Dof} of 1.386 while the Gaussian, Lorentzian and Exponential profiles have fit values of 1.396, 1.396 and 1.391 respectively so the choice of profile was not critical. We use de Vaucouleurs profile but note that the difference in fit quality for such faint sources is minimal.

In principle, the variation of profile brightness at large radius could influence pair finding. However, for $25 < V < 26$ sources we only search for pairs on scales $\theta > 0.8''$. The average de Vaucouleurs intensity for simulated sources at this distance is $2.3 \times 10^{-4} \text{ s}^{-1}$ while the GOODS noise threshold is $4.2 \times 10^{-3} \text{ s}^{-1}$. This value is smaller for all dimmer sources at their respective minimum pair distance (see section 6). The influence on pair-finding is largest for the de Vaucouleurs profile that we have chosen to use and even here it does not greatly affect our final results. Intensities of 5% of the threshold will have minimal influence on the detection. We plot the intensity of idealized de Vaucouleurs, Lorentzian, Exponential and Gaussian profile source with $V \approx 25.5$ and typical detection area in Fig. 4. All other profiles drop off faster than the de Vaucouleurs profile on the pertinent distance scales. The tails at such scales must be minimally important.

3.2 Simulated Source Distribution

Our simulated catalogs are designed to match the magnitude, detection area and ellipticity distributions of GOODS and the UDF. We produced many simulated images using different input distributions until the output catalogs matched the data.

We start by using a broken exponential magnitude distribution in the *V* band:

$$P(V) \propto \Theta(V - V_{max}) e^{\eta V} \quad (8)$$

$$\eta = \begin{cases} 0.92, & \text{for } V < 27.5 \\ 0.72, & \text{for } V > 27.5 \end{cases} \quad (9)$$

where $V_{max} = 29.5$ for GOODS and 31 for UDF.

When determining the width of a source, we scale each source so that it can be seen above the background intensity threshold, T .

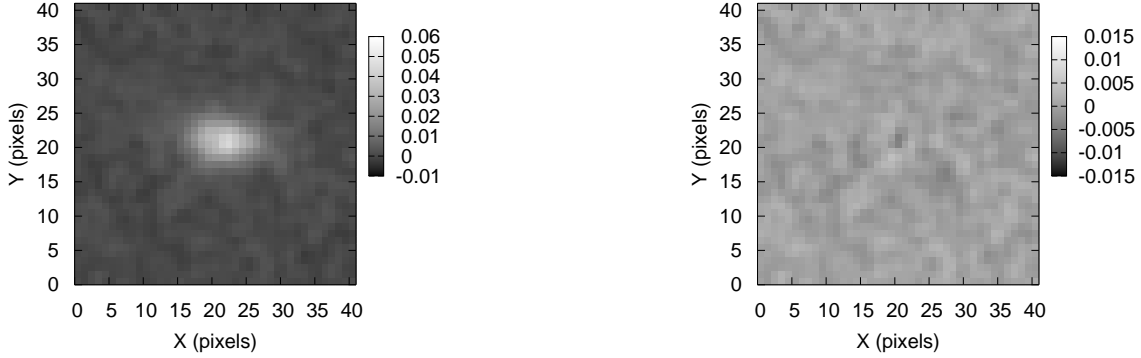


Figure 3. A typical source profile from real GOODS data (left) and the residuals left by a de Vaucouleurs fit (right).

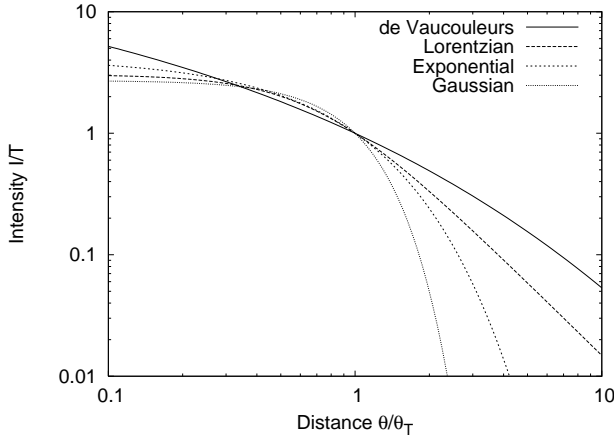


Figure 4. The radial profiles of a simulated $V \approx 25.5$ source using the de Vaucouleurs, Lorentzian, exponential and Gaussian fits. The total intensity within $\theta_T \approx 0.1''$ is constant. The de Vaucouleurs tail is the largest, but it is small at pair separation scales of $\theta_{min} \approx 8\theta_T$.

In the absence of a PSF or ellipticity our sources would have the de Vaucouleurs intensity profiles:

$$I(r) = \frac{I_0}{8! \pi r_0^2} e^{-\left(\frac{r}{r_0}\right)^{1/4}} \quad (10)$$

where I_0 is just the total integrated intensity of the source.

The term r_0 determines the width of our sources. We must make a series of variable transformations to produce a distribution of input r_0 's that leads to an accurate distribution of detected output widths. We start by noting that for an appropriately bright and small source, there is some r_T such that $I(r_T) = T$. The size of the source that we are interested in is the area that exceeds the threshold, πr_T^2 . We define a normalized area above the threshold, A_T , and a normalized area $A_0 \propto r_0^2$. Relating the two tells of how to relate the input source width to the detected source area:

$$T = \frac{I_0}{8! \pi r_0^2} e^{-\left(\frac{r_T}{r_0}\right)^{1/4}} \quad (11)$$

$$A_0 \equiv \frac{8! T \pi r_0^2}{I_0} = e^{-\left(\frac{r_T}{r_0}\right)^{1/4}} \quad (12)$$

$$A_T \equiv \frac{8! T \pi r_T^2}{I_0} = A_0 \log^8(A_0) \quad (13)$$

$A_T = 0$ when $A_0 = 1$, because sources more diffuse than this have central luminosities below threshold. We only make sources with $0 < A_0 < 1$. This function has sharp, undesirable behavior near its minimum at $A_0 = e^{-8}$. Using the variable transformation $\alpha = \log(A_0)$ we can make a smoother, manageable function which we Taylor expand around the maximum at $\alpha = -8$.

$$A_T = \alpha^8 e^\alpha \approx e^{-8} 8^8 \left(1 - \frac{1}{16}(\alpha + 8)^2\right), \quad (14)$$

which we can invert to determine a range on the parameter α :

$$\alpha_T = -8 \pm \sqrt{16 - \frac{2 e^8}{8^7} A_T} \quad (15)$$

At least 10 pixels must be above threshold or $\pi r_T^2 \geq 10$. This yields a range on α for which $A_T > 10 \frac{8! T}{I_0}$:

$$-8 - 4\sqrt{1 - 72 \frac{T}{I_0}} < \alpha < -8 + 4\sqrt{1 - 72 \frac{T}{I_0}} \quad (16)$$

We ignore sources with $I_0/T < 72$ as they are below our detection threshold. After much experimentation, we find that we can reproduce the actual area distribution of sources best if we select alpha from a uniform distribution in the bounds:

$$-9 - 4\sqrt{1 - 115 \frac{T}{I_0}} < \alpha < -9 + 4\sqrt{1 - 115 \frac{T}{I_0}} \quad (17)$$

Finally, we make our sources ellipses with random orientations. The intrinsic ellipticity is chosen as uniform between 0 and 0.9 which reproduces the ellipticity distribution after processing. The position of each source is uniform and random except for the 'partner' sources described in subsection 3.7.

3.3 PSF Simulation

After producing idealized sources we must use an accurate PSF so that small sources are properly blurred and small angle correlations resemble those of the actual image. We cannot use a separate PSF for the roughly 120,000 sources in each of several hundred simulations, so we use a single PSF over our entire field and convolve the simulated image using the FFTW algorithm (Frigo & Johnson 2005).

The PSF is constructed using the ‘Tiny Tiny’ program designed to simulate HST PSFs (Krist 1995). To simulate an average galaxy in the GOODS fields, we assume a power law source spectrum with spectral index $n = -0.1$. We average together 100 PSFs at random positions on each of the two ACS chips and include $0.007''$ of jitter. We apply the electron diffusion PSF in the Tiny Tim documentation taking care to modify the pixel size to $0.03''$. The final PSF has a fitted width that is roughly 0.98 times that of the average fitted width of a random sample of 10 point-like sources.

3.4 Simulated Noise

In all simulated images, we use background noise that approximates the small scale structure of our image and matches the gross statistical properties of the noise in our data. The noise is a field of Gaussian random numbers with variance proportional to the inverse of a weight image at each pixel. To simulate drizzling and cosmic correlation, we convolve this noise with a modified top hat function with bin values proportional to the fraction of their area that a 0.98 pixel radius circle would fill. We scale the standard deviation of the Gaussian field so that we match the roughly 0.0025sec^{-1} rms calculated by Oextractor in GOODS. Our RMS in UDF is roughly 0.0007sec^{-1} .

With these constraints, the number of counts in the simulated negative image (image multiplied by -1 so that sources are ignored by Oextractor) is equal to counts in the negative image when we lower the detection threshold to 1.4σ (to increase counts to roughly 200). Zodiacal light, sunlight scattered off of dust, is the largest background for HST observations (Bernstein et al. 2002), and our background is roughly consistent with a constant zodiacal glow.

3.5 Comparison of Simulated Image Catalogs with Data Catalogs

The above procedures produced catalogs with similar distributions in V magnitude, detection area and ellipticity as those in the actual GOODS and UDF catalogs as shown in Fig. 5. The number of sources within any magnitude band was within a few percent of the observed value, and that the area and ellipticity distributions are similarly close to those observed in the GOODS field.

3.6 False Detections in Simulated Images

The detection algorithm in section 4 was guided by our study of false detections in simulated images. To find false sources, we compared the positions of detected sources to those of actual sources in our input image. We made a catalog of detected sources that were more than $0.3''$ (ten pixels) away from actual sources (as defined by an input catalog of sources). We never include pairs closer than this in our correlation function calculation. These potential detection areas cover a total of around 10 percent of the detection area. Increasing the distance at which we are willing to associate a detection with an input source beyond $0.3''$ decreased the number of false detections at a rate consistent with the decrease in area that was ‘‘far from a source’’. This indicates that false detections are not strongly clustered around sources on scale greater than $0.3''$. We find roughly 270 false sources in GOODS South, 0.5% percent of our total sources. This fraction is roughly constant across magnitude.

3.7 Simulated Clustering

In order to evaluate our ability to measure an intrinsic correlation function, we must see how well we measure the correlation function in simulated clustered datasets. To make these datasets we start with an unclustered data set and assign each source n_p partners where the distribution of n_p is:

$$P(n_p) = \frac{e^{-n_p/n_0}}{n_0}; n_0 = \rho_0 \int_{0.2''}^{10''} \left(\frac{\theta}{\theta_0} \right)^{-2.5} 2\pi\theta d\theta \quad (18)$$

where $\theta_0 = 0.432''$ ($0.27''$) for GOODS (UDF).

These clustered sources increases the total number of sources by 50% (33%). Each extra source is assigned a separation angle, θ , from its parent with a distribution:

$$P(\theta) \propto \theta^{-1.5} \quad (19)$$

Between a minimum θ of $0.2''$ ($0.1''$) in GOODS (UDF) and a maximum θ of $10''$. We pick a uniformly distributed random position angle ϕ .

This method produces power law distributed clumps but because of clump-clump correlations does not produce perfect power law behavior. Nor does it produce an exact match to the observed correlation function. We use these simulations only to study how well our measurement algorithm recovers an intrinsic correlation.

4 CATALOG PRODUCTION

Attempts to measure $w(\theta)$ and $\xi(r)$ in bright galaxy surveys are rarely confused about what is being counted. Bright $r < 22$ galaxies are physically distinct ‘island universes’, and although they are observed to collide and merge, the autocorrelation statistics are not seriously hindered by decisions about whether or not to count a comparatively rare interacting pair as one galaxy or two. However, when considering the FSCF in our sample, we quickly realize that θ_0 is only a few times larger than the physical size of the sources and the resolution of the observations. This implies that we must be scrupulous in defining sources and consistently use the same definition when comparing with simulations of galaxy formation.

4.1 Source Extraction

When making our catalogs for FSCF study, we designed a source extraction routine geared to look for faint, compact sources and deblend aggressively. In exchange for this increase in performance, we allowed for around 0.5% false sources that the more conservative GOODS catalog lacks.

We started with the catalog procedures used by the GOODS team and modified them to look for faint sources and pairs. In making their catalogs, the GOODS team used a modified version of the SExtractor (Bertin & Arnouts 1996) program called Object Extractor (Oextractor) that is designed to better extract faint sources near bright neighbors by modifying the noise floor in these areas. Oextractor also avoids including spurious noise in the area of a source as part of that source. We borrowed their code to produce our own catalog.

We modified the GOODS team’s procedures at several stages. Our most distinct change in method from the GOODS team was to use the V band (F606W) instead of the z band (F850LP). Using any reasonable SExtractor parameters designed to find faint sources, we find more GOODS sources in the V band. For our particular set of parameters, we found 56088 source in V band and only 29601 in

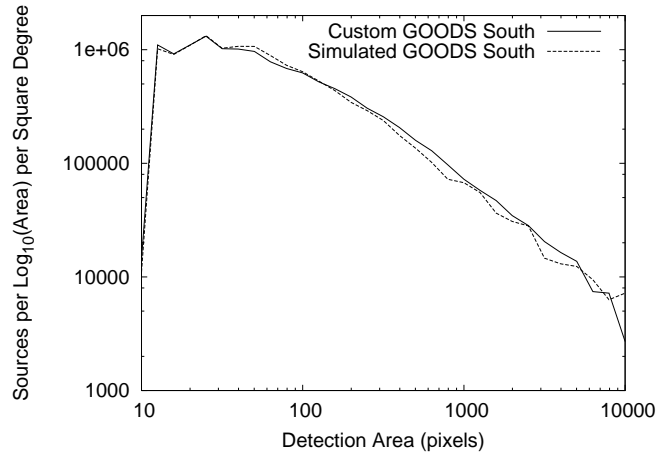
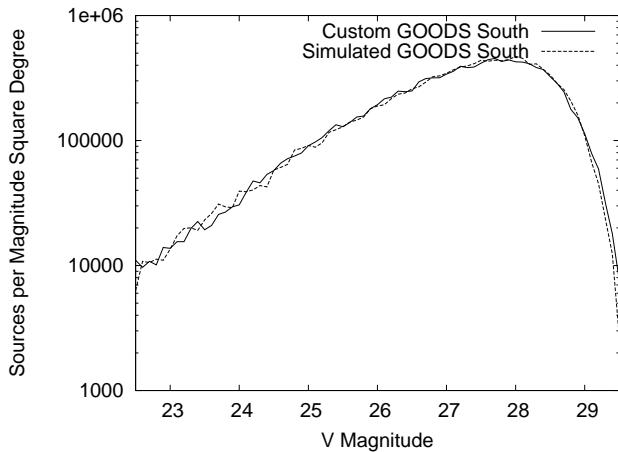


Figure 5. The magnitude (left) and area (right) distributions of actual and simulated GOODS data.

	Standard GOODS Catalog	Custom Catalog
WEIGHT_TYPE	MAP_RMS	MAP_WEIGHT
Filtering FWHM (Pixels)	5.0	1.5
DETECT_THRESH	0.6	1.7
DETECT_MINAREA	16	10
DEBLEND_NTHRESH	32	16
DEBLEND_MINCONT	0.03	0.03

Table 2. The standard and custom GOODS SExtractor parameters.

z. This suggests that many faint source are many blue star forming regions. We also changed the actual Oextractor detection parameters to better find faint, small sources. Our changes are summarized in Table 2. One should note that the GOODS team used RMS images (not publicly available) that are normalized differently from our weight images and that, accounting for this difference, our DETECT_THRESH is roughly equivalent to theirs.

We arrived at these numbers by examining the correlation function of the $27 < V < 28$ sources in uncorrelated simulation images, the number of detections in real images and the number of false counts in simulated images. To determine a filtering FWHM, we ran Oextractor with different Gaussian filters of width between 1 and 5 pixels ($0.03'' - 0.15''$) to produce catalogs from simulated uncorrelated data. The correlation function of these catalogs would ideally be zero for all values of θ , but we found that it became significantly negative at distances of roughly 3 times the FWHM. Running Oextractor without filtering or while using only a small filter causes the correlation function to become very large on scale less than $0.2''$. A FWHM of 1.5 pixels was the smallest we could use without introducing this small angle peak.

We again used this correlation function to study the DEBLEND_NTHRESH-DEBLEND_MINCONT parameter space. We qualitatively found the parameters which minimize spurious deblending, manifested by a large correlation of what should be uncorrelated data at separations of roughly $0.1 - 0.3''$, without hindering our effective resolution, manifested as a suppression of $w(\theta)$ on scale of $0.2'' - 0.5''$. Our final choice was identical to Benitez et al. (2003).

We examined the 2 dimensional space of DETECT_MINAREA and DETECT_THRESH using total counts from the real image and false counts in a simulated image. The PSF is roughly 3 pixels wide, so we centred our search around DETECT_MINAREA ≈ 9 . We tried every integer value between 6

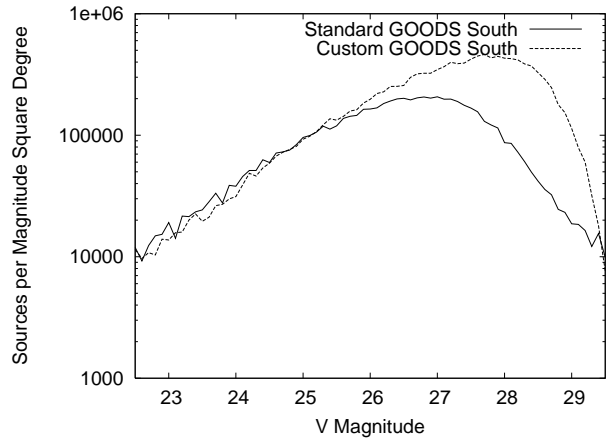


Figure 6. The magnitude distribution in the standard and custom GOODS South catalogs. The custom GOODS catalog contains nearly twice as many sources.

and 20 pixels. Roughly speaking, we wanted to focus on aggressive 5σ detections. For DETECT_MINAREA = 9, a 5σ detection corresponds to DETECT_THRESH ≈ 1.7 . We tested every 0.1 interval of DETECT_THRESH between 0.6 and 3. Our goal was to obtain the largest number of detections with 99.5% purity. Our final setting of 10 pixels at 1.7 yields an average of 60,000 detections in a simulated GOODS South data set with 270 false detections.

Our source extraction procedure detects only 51 negative sources in GOODS South and an average of about 270 false detections in simulated images (as described in section 3). This catalog raises the total number of counts from 29601 to 56088 in GOODS South. In addition, Fig. 6 shows that we improved completeness of extended sources from roughly $V = 26$ to $V = 27.5$. To justify our previous claim that the V band is preferable for detecting many faint sources, we note that we detect only 29488 sources and 67 negative sources on the z band with the above parameters.

4.2 Masking

Our source extraction methods fail in two areas of our images, so we masked these areas out separately. High noise near the edges of

our images produce a large number of correlated pairs. Improper background subtraction and real structure near bright sources produced many suspect pairs.

Near the edges of our images, effective exposure time drops off, and the background noise becomes large. These areas looked qualitatively different from the rest of the image and produced a disproportionate number of close pairs, so we removed them from our images. To do this, we convolved the weight images with a 30 pixel ($0.9''$) top hat and excised all areas in the original weight and science images where the weight in this convolved image was less than 40,000. These masked area amounted were concentrated almost entirely near the edges of the images and amounted to roughly 2% of the original images.

Bright ($V < 21$) sources provide two separate problems. First, errors in background subtraction from these sources affect significant area and are not accounted for in our source extraction procedures. Second, our aggressive deblending means that a small number of bright, nearby sources with complex structure can be split into many faint pairs and significantly influence the overall correlation function. We are only interested in studying faint sources that are not obviously associated with a bright source. To mask out these bright sources, we reject all sources contained in ellipses which are four times the area of the bright source. These masked areas amounted roughly 2% of the original images.

4.3 Characterizing the Catalogs

Our catalogs contain many faint sources that are small in extent and separation. The example sources in Fig. 7 range in magnitude between $V = 26.31$ and $V = 27.49$ and in diameter between $0.1''$ and $0.3''$. The separation lengths between detected sources range between $0.3''$ and $1.2''$.

These are 3.5 – 2.5 magnitudes dimmer than those used in large scale studies like SDSS. Converting from SDSS r band to HST V band is an imprecise technique. We observe that sources have $B - V$ of roughly 1.1 and make the rough conversion between detection bands via (Jester et al. 2005):

$$r = V - 0.42(B - V) + 0.11 \approx V - 0.36 \quad (20)$$

Given the approximate nature of the spectra, this should be taken as only a rough conversion, but the SDSS cutoff magnitude of $r = 22.5$ is roughly equivalent to a GOODS/UDF $V = 22.9$ cutoff, two magnitudes brighter than the dimmest sources we use.

We also work on much smaller scales. Typical source separation in SDSS were $100''$, resolution limits source size to $1.4''$ and statistics limited their source separation to $10''$. Our typical source separation is roughly $5''$, our resolution is $0.12''$ and we see pairs with $0.3''$ separation.

We place these numbers in an astrophysical context in table 3. For reference, M31 has an absolute magnitude of roughly $V = -20$ and the bulk of its luminosity is from a disk roughly 20 kpc across.

Finally in Table 4, we note the number sources, $10''$ pairs and $1''$ pairs. The crucial number is the number of $1''$ pairs. The Poisson noise of this number gives us a rough idea of how well we can measure our subarcsecond correlation function and shows that we cannot avoid at least a few percent error.

z	Absolute V	Arcsecond Linear Size (kpc)
0.1	-11.3	1.8
0.2	-12.9	3.3
0.5	-15.3	6.1
1	-17.1	8.0
2	-19.0	8.5
5	-21.4	6.4

Table 3. The absolute magnitude of a source with apparent magnitude 27 (in an appropriately blueshifted V band) and physical distance corresponding to $1''$ at various redshifts.⁷

Sample	Subsample	Sources	$10''$ pairs	$1''$ pairs
GOODS South	$25 < V < 26$	6266	10653	591
	$26 < V < 27$	12282	41049	1514
	$27 < V < 28$	18356	92252	1885
GOODS North	$25 < V < 26$	6535	11405	626
	$26 < V < 27$	12080	36603	1442
	$27 < V < 28$	18016	81140	2015
UDF	$27 < V < 28$	1339	6154	141
	$28 < V < 29$	2111	15394	227

Table 4. The number of sources, $10''$ pairs and $1''$ pairs for each subsample.⁷

5 CORRECTING MEASUREMENT ERROR IN THE CORRELATION FUNCTION

For large angle correlation functions, nonuniform survey depth is usually the major threat of measurement error. After masking out the edges of the survey (see subsection 4.2) we have relatively uniform surveys and particularly very little survey depth structure on the arcsecond scale. In addition, conspicuous causes of ‘false sources’ such as diffraction spikes and cosmic rays near the edge of the image where drizzling is not effective are again cleanly removed by this masking.

Proper deblending of distinct objects and improper deblending of single source is our main source of measurement error. We examine this problem from two perspectives. First, we estimate a correlation function caused by imperfect measurement techniques using intrinsically unclustered simulated data. Secondly, we estimate our ability to measure actual clustering using simulated clustered data.

5.1 Measurement-Induced Correlations in Uncorrelated Data

Our approach is an extension of the statistical method for evaluating the correlation function introduced by Hamilton (1993). Specifically, to minimize the effects of nonuniform weighting and uncertainty in the zero point of $w(\theta)$ we use a combination of two of Hamilton’s estimates of the correlation function:

$$1 + w_{est}(\theta) = \frac{\langle DD \rangle \langle RR \rangle}{\langle RD \rangle^2} \quad (21)$$

$$1 + w_{est}(\theta) = \frac{\langle DD \rangle}{\langle RR \rangle} \quad (22)$$

Here, $\langle DD \rangle$ is the simple estimate of the data-data correlation function taken as a series of delta functions representing each pair separation. $\langle RR \rangle$ is the random-random correlation function of many (in our case 40) random fields emulating the appropriate dataset, and $\langle RD \rangle$ is the correlation of the appropriate data field with its corresponding random fields. We convolve $\langle RR \rangle$ and $\langle RD \rangle$ with a Gaussian filter with angular width



Figure 7. A typical singleton, pair and cluster of faint source. These sources are from the GOODS South field and range in magnitude between $V = 26.3$ (the second lowest source in the cluster) and $V = 27.5$ (the singleton).

	GOODS	UDF
$25 < V < 26$	0.8	—
$26 < V < 27$	0.55	—
$27 < V < 28$	0.4	0.5
$28 < V < 29$	—	0.3

Table 5. θ_{min} in GOODS and the UDF.

$0.1''$ to produce continuous functions. We normalize each function by a factor of roughly σ_0^2 such that it converges to unity at large angles.

The first method excels at reducing error due to survey nonuniformity. But at small angles, resolution and source size reduce $\langle DD \rangle$ and $\langle RR \rangle$, but not $\langle RD \rangle$, and the estimate of $w(\theta)$ is artificially damped. The second method does not counter survey nonuniformity as well as the first, but the damping in $\langle DD \rangle$ and $\langle RR \rangle$ cancel to first order to give a more accurate measurement at small angles. Therefore, we use the first method for $\theta \geq 2''$ and the second method for $\theta < 2''$.

$$1 + w_{est}(\theta) = \frac{\langle DD \rangle}{1 + w_M(\theta)} \quad (23)$$

$$1 + w_M(\theta) = \frac{\langle RD \rangle^2}{\langle RR \rangle}, \text{ for } \theta > 2'' \quad (24)$$

$$\langle RR \rangle, \text{ for } \theta < 2''$$

where we have defined w_M , the measurement-induced correlation function, for our own convenience.

To first order, w_M is the correlation function one would observe from a naive $\langle RR \rangle$ measurement of uncorrelated sources due to survey geometry and improper deblending. This function can be positive if a single source is improperly deblended or if dim sources are enhanced by the tail of a bright source. It can be negative if two sources are separated by less than their angular extent or the resolution of the instrument. In Fig. 8, we compare the observed data-data correlation function $1 + w_O = \langle DD \rangle$ and $1 + w_M$ (each convolved with a $0.1''$ filter). w_M is always smaller than w_O , but on small scales, it is generally within an order of magnitude of w_M and must be handled intelligently to prevent significant systematic error.

We use our estimation of the measurement correlation function in Fig. 8 to choose θ_{min} below which we do not study the correlation function. We define θ_{min} as roughly $0.1''$ greater than the angle where w_M approaches unity or where it becomes negative. This corresponds roughly to the source size, below which our simple source profile assumptions should become important.

	GOODS		UDF	
	κ	λ	κ	λ
$25 < V < 26$	1	0.8	—	—
$26 < V < 27$	1	0.3	—	—
$27 < V < 28$	0.64	0.0	1	-0.4
$28 < V < 29$	—	—	0.89	-1.2

Table 6. λ and κ in used to reproduce input correlation functions in simulated data.

5.2 Correcting Measurement Error

For large scale correlation functions of bright sources, the naive observed correlation function, $w_O = \langle DD \rangle - 1$, and the physical correlation function, $w_P \approx w_{est}$, are simply related:

$$1 + w_O = (1 + w_P)(1 + w_M) = 1 + w_P + w_M + w_P w_M \quad (25)$$

But because we are measuring the correlation function on scales similar to the PSF and source size, we must adapt this method to account for these effects. We find that the suppression of the correlation on small scales is dependent on the amplitude of the correlation function and the magnitude of the sources being measured. We use a fitting model that accounts for these dependencies and is accurate well within our statistical error bars.

We must relate the known w_O and w_M to an unknown w_P . For small values of w_P and w_M , w_O should equal $w_M + w_P$ since there is only perturbative clustering and measurement error. To make a first order approximation when w_P and w_M are not both small we use the following model:

$$1 + w_O = 1 + w_P + w_M + \lambda w_P w_M \quad (26)$$

For the standard correlation function measurement, $\lambda = 1$ to make this a product. But we find that varying λ is a convenient way to account for nonlinear effects of measurement error in crowded fields. The λ term is only significant on small scales where both w_P and w_M are large.

In addition, we find that for incomplete samples, we underestimate the correlation function even at large separations. We introduce parameter κ to correct for this effect in faint, incomplete samples ($27 < V < 28$ in GOODS and $28 < V < 29$ in UDF):

$$1 + w_O = 1 + \kappa w_P + w_M + \lambda w_P w_M \quad (27)$$

Using the κ and λ parameters, we can reconstruct w_P from w_O and w_M using:

$$1 + w_P = 1 + \frac{w_O - w_M}{\kappa + \lambda w_M} \quad (28)$$

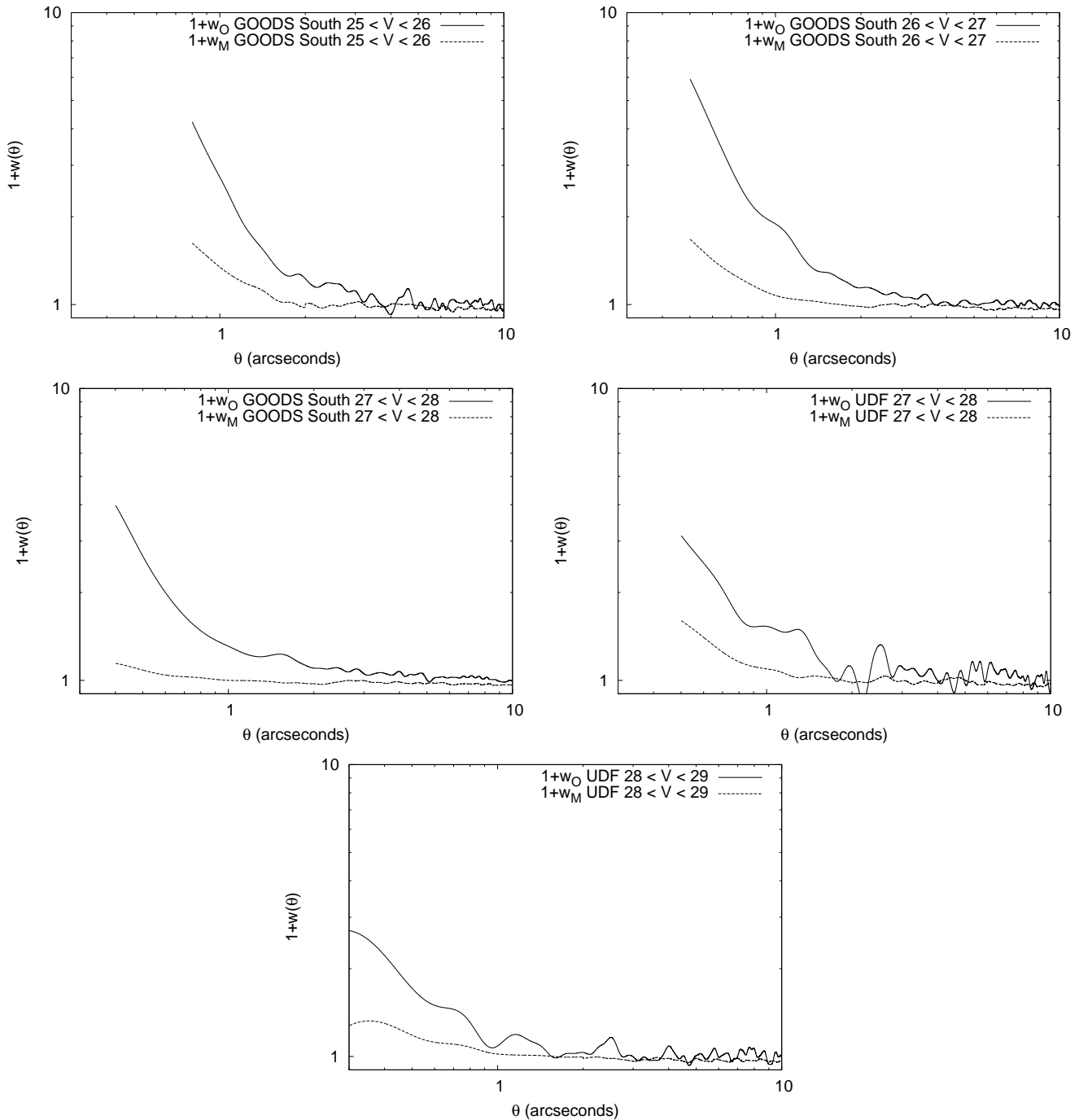


Figure 8. We compare w_O , the naive observed correlation function in our data and w_M , the correlation function induced on a random field of sources via spurious deblending, in the GOODS South field and the UDF.

as shown in Fig. 9 for simulated clustered data. In these plots we show $0.02 + w$ to facilitate logarithmic plotting. We calculate w_P using the known positions of sources in our simulated clustered images. The fits in Fig. 9 guided us to use this parameterization.

Models which related higher powers of w_P and w_M to w_O did not improve our ability to reconstruct the input correlation function significantly. Our simple λ fit allowed us to find simulated w_p with precision much greater than the statistical fluctuations in a single GOODS or UDF measurement, so it is sufficient for our purposes. More precise models may be employed for future work. The essen-

tial requirement for any such method is that close pair suppression vary with the amplitude of w_P .

6 THE ESTIMATED CORRELATION FUNCTION

We employ a maximum likelihood estimation technique to measure the correlation function, $w(\theta)$ without binning in θ . Mathematically, not binning is equivalent to binning very finely so that each in has either one or zero sources in it. If we assume a Poisson

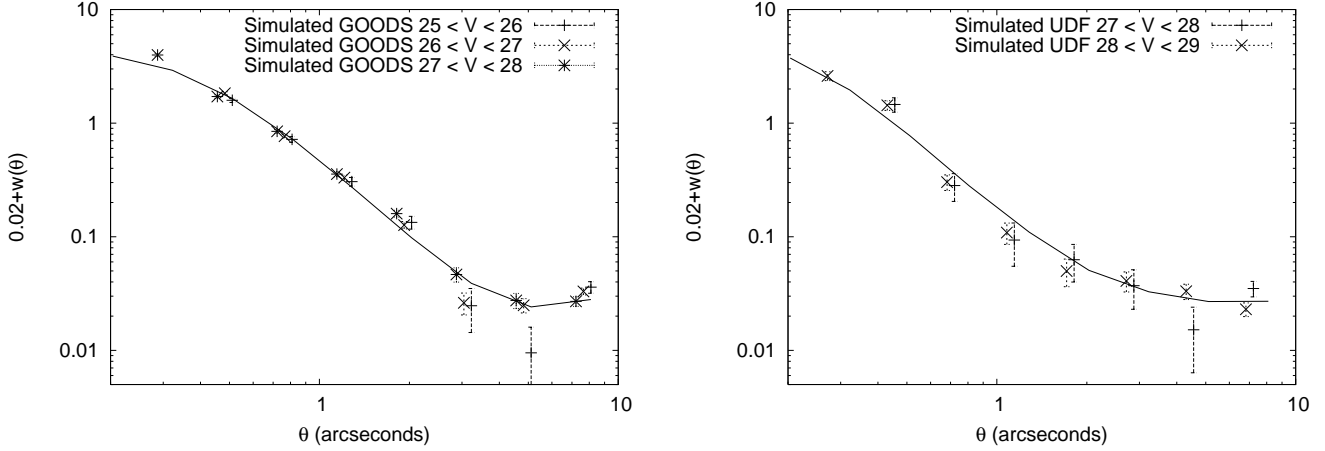


Figure 9. w_P (lines) and $(w_0 - w_M)/(\kappa + \lambda w_M)$ (datapoints) in simulated GOODS (left) and UDF(right). We obtain w_P by finding the correlation function in the input catalogs we use to make our clustered simulated images.

distribution in each bin, the likelihood of a particular realization would be:

$$L(\sigma_0, \theta_0, \Gamma) = \prod_{i=1}^n e^{-\mu_i} \mu_i^b \quad (29)$$

where b is equal to the number of pair correlations within this angle bin (either 0 or 1) and μ_i is equal to the expected number of pairs in this bin:

$$\mu_i = \sigma_0^2 (1 + w_M(\theta_i) + (\theta_i/\theta_0)^{-\Gamma} (\kappa + \lambda w_M(\theta_i))) A 2\pi\theta_i \delta\theta \quad (30)$$

where A is the area of the sample and $\delta\theta$ is the bin width, constant and small enough so that $\mu \ll 1$.

Implicitly, we have some maximum and minimum θ defined as $\theta_{max} - \theta_{min} = n \delta\theta$. Hence:

$$\log(L) = \sum_{i=1}^n (-\mu_i + b_i \log(\mu_i)) \quad (31)$$

$$= -\sum_{i=1}^n \mu_i + \sum_{pairs} \delta\theta + \quad (32)$$

$$\sum_{pairs} \log(\sigma_0^2 (1 + (\theta_i/\theta_0)^{-\Gamma} (\kappa + \lambda w(\theta_i))) 2\pi\theta_i)$$

In the continuous limit,

$$\log(L) = -\int_{\theta_{min}}^{\theta_{max}} \mu(\theta) d\theta + \sum_{pairs} \log(\mu(\theta)) + \text{constant} \quad (33)$$

where we have abbreviated the sum involving only $\delta\theta$ as merely a constant which will be unimportant in the maximization process.

We introduce a continuous version of μ :

$$\mu(\theta) = \sigma_0^2 (1 + w_M(\theta) + (\theta/\theta_0)^{-\Gamma} (\kappa + \lambda w_M(\theta))) A 2\pi\theta \quad (34)$$

We maximize L over σ_0^2 , Γ and $w_1 = (\theta_0)^\Gamma$. To find the error bars for each parameter, we perturb its value, maximize over the remaining parameters and use the second derivative of this marginalize likelihood to estimate 1σ errors.

6.1 Fit Values

We present our final values in the GOODS North field, the GOODS South field and the UDF in Table 7. The systematic error bars are

	$w(1'')$	θ_0
$25 < V < 26$	$0.889 \pm 0.041 \pm 0.088$	$0.955 \pm 0.077 \pm 0.038$
$26 < V < 27$	$0.511 \pm 0.016 \pm 0.052$	$0.758 \pm 0.027 \pm 0.031$
$27 < V < 28$	$0.298 \pm 0.076 \pm 0.030$	$0.598 \pm 0.091 \pm 0.024$
$28 < V < 29$	$0.113 \pm 0.052 \pm 0.009$	$0.479 \pm 0.035 \pm 0.016$

Table 9. Best global estimates of $w(1'')$ and θ_0 assuming $\Gamma = 2.5$.

explained in subsection 6.2. The results are consistent. Particularly, our GOODS results for $27 < V < 28$ agree with our UDF results for the same sources.

Comparison with previous results is necessarily indirect. Vilumsen et al. (1997) produced the most comparable measurement, but used r band limits rather than V band ranges. As a point of reference, we see that our $25 < V < 26$ measurement and their $20 < r < 26$ are within statistical error bars for $\theta > 1''$. More broadly, we agree that $w(\theta) \approx 0.1$ for $\theta > 1''$ for these faint sources. It is our probing down to $w(\theta)$ for $\theta < 1''$ that gives us a significant measurement.

The GOODS North and South results are in good agreement. So we make a final estimate combining the two datasets to minimize statistical noise. We then have our best estimate of the correlation function in each of the four magnitude bins in Table 8. In the $27 < V < 28$ bin we use UDF data expressing our preference for statistical uncertainty over systematic uncertainty.

These results are consistent within computed error of a $\Gamma = 2.5$ in all cases. Assuming this value gives us slightly different values of θ_0 in Table 9. The correlation length as a function of limiting magnitude V is well fit by:

$$\theta_0(V) = 10^{-0.1(V-25.8)} \text{arcsec}; \quad 26 < V < 29 \quad (35)$$

This is a factor of 40 larger than what we would expect from the extrapolation of a purely gravitational correlation function in equation 4.

We plot our results in Fig. 10 with the best $\Gamma = 2.5$ fit. We also plot the $\Gamma = 0.7$ fit to show that extending the SDSS power law to small scales vastly underestimates the number of close pairs. Note that we are plotting $0.02 + w(\theta)$ for GOODS and $0.1 + w(\theta)$ for UDF, because it allows for slightly negative points to be included in a log-log plot. Also note that the $\Gamma = 0.7$ fits are of $(\theta/\theta_0)^{-0.7} + \delta$, where δ is an independently fit parameter. δ is necessary, because

	$w(1'')$	θ_0	Γ
GN 25 < V < 26	$0.83 \pm 0.05 \pm 0.12$	$0.93 \pm 0.10 \pm 0.04$	2.48 ± 0.37
GS 25 < V < 26	$0.92 \pm 0.05 \pm 0.10$	$0.97 \pm 0.11 \pm 0.04$	2.55 ± 0.15
GN 26 < V < 27	$0.536 \pm 0.019 \pm 0.053$	$0.775 \pm 0.043 \pm 0.031$	2.45 ± 0.17
GS 26 < V < 27	$0.508 \pm 0.020 \pm 0.051$	$0.759 \pm 0.042 \pm 0.031$	2.45 ± 0.17
GN 27 < V < 28	$0.36 \pm 0.015 \pm 0.10$	$0.649 \pm 0.035 \pm 0.074$	2.38 ± 0.14
GS 27 < V < 28	$0.234 \pm 0.013 \pm 0.067$	$0.549 \pm 0.033 \pm 0.074$	2.42 ± 0.20
UDF 27 < V < 28	$0.296 \pm 0.053 \pm 0.029$	$0.60 \pm 0.10 \pm 0.02$	2.41 ± 0.63
UDF 28 < V < 29	$0.087 \pm 0.024 \pm 0.009$	$0.438 \pm 0.042 \pm 0.016$	2.96 ± 0.50

Table 7. $w(1'')$, θ_0 (in arcseconds) and Γ for GOODS North (GN), GOODS South (GS) and the UDF.

	$w_{1''}$	θ_0	Γ
25 < V < 26	$0.946 \pm 0.034 \pm 0.094$	$0.979 \pm 0.084 \pm 0.038$	2.58 ± 0.28
26 < V < 27	$0.520 \pm 0.014 \pm 0.051$	$0.763 \pm 0.030 \pm 0.031$	2.43 ± 0.12
27 < V < 28	$0.296 \pm 0.053 \pm 0.028$	$0.60 \pm 0.10 \pm 0.024$	2.41 ± 0.63
28 < V < 29	$0.087 \pm 0.024 \pm 0.009$	$0.438 \pm 0.042 \pm 0.016$	2.96 ± 0.50

Table 8. Best global estimates of $w_{1''}$, θ_0 and Γ .

different fit Γ 's lead to different σ_0 values and effectively offset $w(\theta)$.

The σ_0 we use slightly undervalues the true density, because we require our fitted $w(\theta)$ to always be positive. In a sense, our σ_0 represents the density of sources if there were no 'extra pairs' due to the correlation function. Given this expected discrepancy, our fitted results are consistent with being slightly less than $n_{sources}/Area$ and we do not print them here.

6.2 Systematic Error

Our methods produce systematic errors related to how our simulations differ from true images. We trace these error to two effects: unrepresentative source profiles and inadequate noise models. The effects manifest themselves as errors in w_M and w_O . If our simulations are accurate, however, the effects should cancel out in our final measurement of w_P . But any discrepancies between our simulations and real images will prevent this cancellation and produce systematic errors in our measured w_P . We set generous upper limits on discrepancies in our estimate of systematic error and find that statistical error is still our major source of noise in θ_0 .

Object Extractor, like Source Extractor, subtracts a background profile from each source so that the faint (below detection threshold) wings of each source do not make the surrounding sources appear brighter. But for both the real and simulated images, this process is imperfect and background subtraction may cause any source in the region surrounding a given source to be recorded as brighter or dimmer than it truly is.

Source profiles are generally larger than PSFs, and we were able to reduce our error in PSF width to at most 2%, so we focus on the source profiles. In subsection 3.1, we noted that the intensity of a typical source is at most 0.05 DETECT.THRESH at the distances at which we search for pairs. This sets an upper limit in the difference between observed and actual luminosity of roughly $|\Delta L/L| = 0.05$.

Source concentration is proportional to:

$$\sigma(L) \propto e^{\eta V(L)} \quad (36)$$

and an uncertainty in L will lead to a localized uncertainty in σ . This localized uncertainty in σ will produce or suppress pairs, directly altering $w(\theta)$ at the scale of the improper background subtraction.

Sample	σ_{bs}	σ_κ	σ_{θ_0}
25 < V < 26	0.038	0	0.038
26 < V < 27	0.031	0	0.031
27 < V < 28 GOODS	0.022	0.070	0.074
27 < V < 28 UDF	0.024	0	0.024
28 < V < 29	0.011	0.011	0.016

Table 10. Systematic errors due to background subtraction.

Applying 0.05 fractional uncertainty in luminosity at the θ_0 scale leads to a background subtraction uncertainty, σ_{bs} , in θ_0 of roughly:

$$\begin{aligned} \sigma_{bs} &= 0.05 \left(1 + w(\theta_0) \frac{\partial \sigma(L)}{\sigma(L)} \frac{\partial \theta_0}{\partial L} \frac{\partial \theta_0}{\partial w} (\theta = \theta_0) \right) \\ &= \frac{0.05 \times 2 \times \eta}{\log(10^{0.4}) \Gamma} \theta_0 \end{aligned} \quad (37)$$

The effect of false detections is twofold. If the detections were randomly scattered throughout the image, the extra 0.5% sources would reduce the correlation function on all scales by 0.5%. Any clustering of these sources could contribute to a positive correlation function. But we do not observe strong clustering of false detections near sources in subsection 3.6 on the scales we probe here. We estimate that false detections are at most twice as likely in the area $\theta < 2\theta_0$. This implies that only about 0.1% of sources would have an extra partner on these scales. In subsection 6.3, we find that roughly 10% of sources have a partner on these scales, so false detections are only a percent level source of error. We neglect their contribution in our systematic error estimate.

A separate source of significant error derives from the use of the incompleteness factor, κ . We use this factor in our GOODS 27 < V < 28 and UDF 28 < V < 29 measurements to counter the effects of incompleteness. The values we use reproduce the input correlation function in our simulation measurements, but we do not understand exactly how incompleteness affects $w(\theta)$. The farther κ is from its ideal value of unity, the more uncertainty our use of κ implies. We assign a fractional uncertainty in κ equal to $0.5(1 - \kappa)$ to produce generous error bars in our measurements of θ_0 in incomplete samples. This leads to an uncertainty σ_κ in θ_0 of:

$$\sigma_\kappa = \frac{0.5(1 - \kappa)}{\kappa \Gamma} \theta_0 \quad (38)$$

We do not apply systematic error to Γ , because Γ is highly

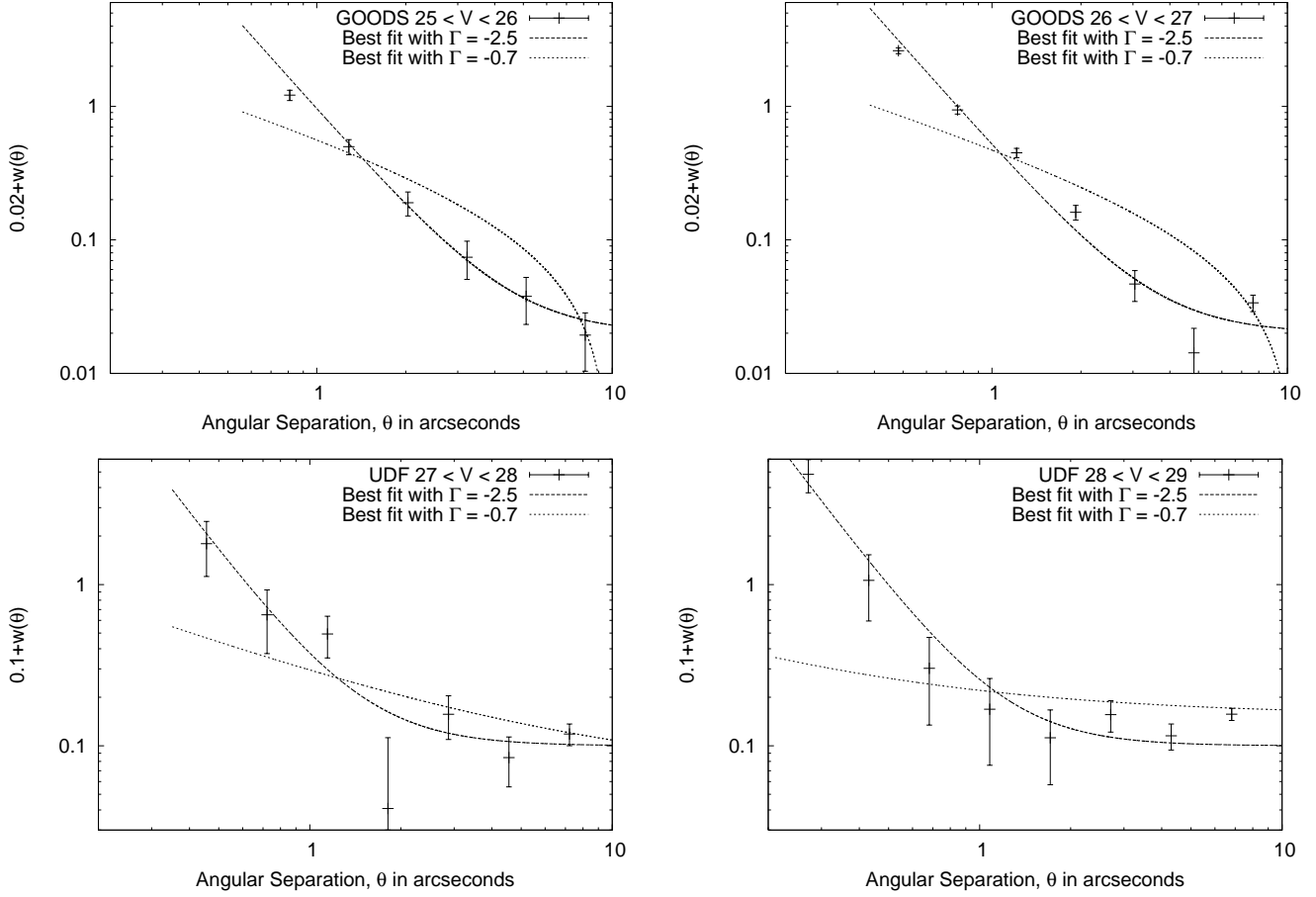


Figure 10. The fitted correlation function in GOODS $25 < V < 26$ (top, left), GOODS $26 < V < 27$ (top, right), and UDF $27 < V < 28$ (bottom, left) and UDF $28 < V < 29$ (bottom, right). We show our best $\Gamma = 2.5$ and $\Gamma = 0.7$ fits. $w(\theta)$ is offset from zero by 0.02 (0.1) for GOODS (UDF) so that slightly negative points can be plotted on a log-log plot. This causes distortion in the plots at large angles. The $\Gamma = 0.7$ fits are actually $(\theta/\theta_0)^{-0.7} + \delta$ fits.

dependent on the small number of close pairs, and random errors dominate systematic errors.

In this paper, we do not address the issue of cosmic variance. While each field is many times larger than our critical distance of roughly one arcsecond, cosmic source densities can vary on large scales and the effect of such variation on small scale clustering is unclear. It is likely that different clusters of sources are separated by cosmological distances along the line of sight. So by taking an angular measurement, we may be averaging out cosmic variance. There is no statistically significant variation in θ_0 , Γ or source density σ_0 between GOODS North and GOODS South, and we have no reason to believe that cosmic variance is a significant effect.

6.3 Multiplicity Fractions

Measuring the fraction of sources in close pairs is another way to study clustering. It allows us to compare the correlation length with the average separation of sources. These fractions also give us detailed estimates of how many pairs we have in the sky.

In Fig. 11 we see $F_1(\theta)$, the fraction of sources with one neighbor within θ of them. In an unclustered sample, we would have:

$$F_{1u}(\theta) = 1 - e^{-\pi\sigma_0(\theta^2 - \theta_{min}^2)} \quad (39)$$

While in a clustered sample, we have:

Sample	σ_0 degree $^{-2}$	θ_0	$N_{pairs}(2\theta_0)$ degree $^{-2}$
$25 < V < 26$	1.4×10^5	$1.06''$	1.6×10^4
$26 < V < 27$	2.8×10^5	$0.880''$	4.3×10^4
$27 < V < 28$	5.0×10^5	$0.64''$	1.1×10^5
$28 < V < 29$	7.8×10^5	$0.493''$	1.3×10^5

Table 11. Integrated source and pair counts (per square degree) in our catalogs. The $V < 27$ sources are taken from GOODS South and the $V > 27$ sources are taken from UDF.

$$F_{1c}(\theta) = 1 - e^{-\pi\sigma_0((\theta^2 - \theta_{min}^2) + \theta_0^\Gamma / (2-\Gamma)(\theta^{2-\Gamma} - \theta_{min}^{2-\Gamma}))} \quad (40)$$

In our samples, the average separation is $3'' < (\pi\sigma_0)^{-1/2} < 8''$. On scales smaller than this, F_1 would go as θ^2 if the samples were unclustered. Instead, in Fig. 11 we see a steep initial rise with many close pairs and then a flattening out at θ_0 as $w(\theta)$ ceases to dominate.

Finally, the F_1 function allows us to estimate the number of pairs that we see on the sky. In Table 11, we see a roughly exponentially increasing number of pairs within $2\theta_0$ as we go to fainter magnitudes which cuts off at $V \approx 28$. The failure to find more high magnitude pairs could be due to the fact that the $V > 28$ pairs would be on scales very near the resolution limit of the instrument. In any event, if we are to use the FSCF with roughly HST-like space telescopes, we must probe faint sources $V > 25$ to get good statistics.

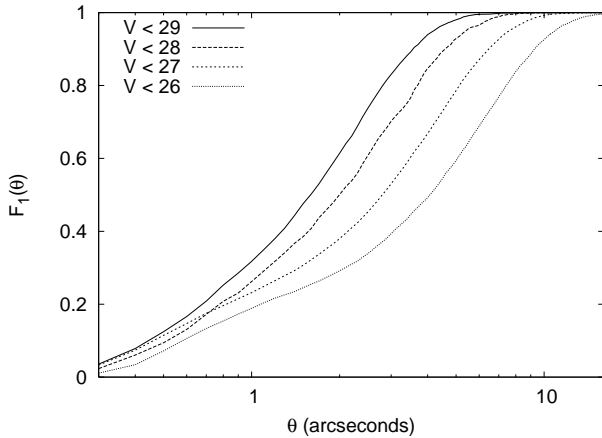


Figure 11. $F_1(\theta)$, the fraction of sources with a partner within θ (left). The $V < 27$ sources are taken from GOODS South and the $V > 27$ sources are taken from UDF.

The integral counts are roughly consistent with:

$$N(V) = 10^{0.4(V-12.7)-0.03(V-25.3)/\text{deg}^2} \quad (41)$$

This formula includes incompleteness in our datasets.

7 DISCUSSION

In this paper we have presented measurements of the two point angular correlation function for faint ($25 < V < 29$) sources. This measurement has been validated by extensive numerical simulation. The observed correlation function is consistent with:

$$w(\theta) = \left(\frac{\theta}{\theta_0(V)} \right)^{-2.5}; \quad \theta_0(V) = 10^{-0.1(V-25.8)} \text{ arcsec} \quad (42)$$

This measurement shows that the FSCF has a much steeper slope and larger normalization than the SDSS angular correlation function for LRGs would suggest if extrapolated. This is not surprising since we are looking at smaller scale physics, at bluer sources and likely at different redshifts. This measurement is not a direct extension of the LRG work, but instead an analogous measurement for a different dataset.

There are many possible uses for this measurement. First, our observation of this galactic scale correlation function can be compared with numerical simulations of galaxy formation that include gravitational clustering, gas dynamics, star formation, etc. In this application it is important that the simulation data be processed in the same way as the observation. Alternately, it is possible to re-analyze this data with a method that derives from the simulation.

Our measurement errors are limited to roughly 10% by the data. They could be reduced substantially with larger samples as has happened with SDSS and the bright source $w(\theta)$. It is unlikely that significantly more deep field type data can be mined from the existing HST instruments. However the Wide Field Camera 3 should be deployed this year and will provide 7 square arcminute exposures of high resolution data with similar limiting magnitudes to the Advanced Camera for Surveys (Kimble et al. 2006). Looking ahead, the James Webb Space Telescope (JWST) is scheduled to launch in 2013 and will provide 5 square arcminute frames with $0.1''$ resolution and a limiting magnitude of at least $K \approx 25$ ($V \approx 30$ for galactic sources) (Gardner et al. 2006). JWST should find many high redshift galaxies. In Table 12, we see

that if we could study the FSCF across many fields to obtain several square degrees of data, we could vastly improve our measurements of $w(\theta)$

Table 12 also shows that several ground-based projects will provide enough data to overcome the small amplitude of the FSCF on arcsecond scales and yield significant measurements. The Dark Energy Survey (The Dark Energy Survey Collaboration 2005) will produce a precise measurement for the $V < 24$ sources that we do not study here. The Panoramic Survey Telescope and Rapid Response System (Pan-STARRS) (Jedicke et al. 2007) and the Large Synoptic Survey Telescope (LSST) (Ivezic et al. 2008) could probe $30,000 \text{ deg}^2$ and $20,000 \text{ deg}^2$ respectively and measure the FSCF of the brighter sources than those we study here with precision of $\approx 10^{-4}$.

But the superior resolution and huge area of possible future space-based surveys makes them the ideal candidates for this method. The Supernovae Acceleration Probe (SNAP) would measure roughly $1,000 \text{ deg}^2$ with a limiting magnitude of approximately 28 (SNAP Collaboration 2005). Destiny has a similar project goal (Benford & Lauer 2006). These enormous surveys would yield FSCF results that directly study $V < 28$ sources on the pertinent subarcsecond scales, reducing the statistical noise we encounter here by a factor of several hundred.

To learn more about these faint sources, we must know their distance. The sources we discuss in this paper are roughly 5 magnitudes too dim for spectroscopy, 3 magnitudes too dim for traditional weak lensing measurements and roughly 2 magnitudes beyond the range where one can rely on training sets to produce accurate photometric redshifts.

Fortunately, lensing enables a new approach to measuring the distance to these sources. Consider first, a field of sources that is gravitationally lensed by large scale structure. The density of a given population of sources will vary inversely with the magnification, μ . But amplification also brings faint sources above the detection threshold, and if the number of sources near the detection threshold goes as $L^{-\beta}$, then the density of total sources goes as $\mu^{\beta-1}$. In practice $\beta \approx 0.8$ and the effects nearly cancel. This and the fact that amplification on cosmic scales is only a few percent make this measurement exceedingly difficult.

But measuring the effect of shear on the FSCF is relatively straight forward and achievable using the large datasets mentioned above. A uniform shear, γ breaks the azimuthal symmetry of the FSCF and, for a power law, the FSCF becomes:

$$w(\theta, \phi) = w(\theta)(1 + \gamma \Gamma \cos(2\phi)) \quad (43)$$

where $w(\theta)$ is the unsheared FSCF, and ϕ is the angle between the source-source separation vector and the axis of shear.

If we have high resolution data with a limiting magnitude of roughly 28, we expect 10^5 close pairs per square degree. With a 1,000 square degree field, we would be statistically limited to measuring to measuring $w(\theta)$ at the 10^{-4} level of precision. A γ of 0.01 could in turn be measured with roughly percent precision. Instead of using this method to measure γ , however, we will use the superior measurements of shear gained from traditional weak lensing of brighter sources with calibrated photometric redshifts to determine the redshift distribution of the faintest sources in the sky.

Cosmic shear is in many ways the most difficult type of lensing measurement to make, and it is likely that the ‘Pair Lensing’ we describe here will follow a similar observational path to traditional weak lensing, first being observed around clusters and galaxies and then being observed in large field.

Dataset	Area (deg^2)	Limiting V Magnitude	θ_{min}	$N_{sources}$	$w_{faint}(\theta_{min})$	$\sigma_{w_{faint}}/w_{faint}$
HST-WFC3	5	27	0.5''	3×10^6	2.8	3×10^{-3}
JWST	5	30	0.5''	4×10^7	0.50	9×10^{-4}
DES	5000	24	1.5''	2×10^8	1.0	1×10^{-3}
Pan-STARRS	30000	26.5	1.5''	1×10^{10}	0.24	2×10^{-4}
LSST	30000	27.5	1.5''	2×10^{10}	0.14	1×10^{-4}
SNAP	1000	28	0.4''	1×10^9	2.8	2×10^{-4}

Table 12. Characteristics of upcoming datasets and their potential to measure $w(\theta)$. The area and limiting magnitude of the HST-WFC3 and JWST are estimated, and these datasets will not be contiguous or uniform surveys. For JWST, we estimate the limiting V magnitude given a $K \approx 25$ limit and galactic sources. θ_{min} is an estimated minimum θ at which we could reasonably make $w(\theta)$ measurements and is equal to roughly three times the PSF width. $w_{faint}(\theta_{min})$ is the size of the correlation function in the faintest single magnitude bin assuming Eq. 42 holds. $\sigma_{w_{faint}}/w_{faint}$ is the fractional statistical uncertainty in this measurement assuming we bin pairs with $\theta_{min} < \theta < 1.58 \theta_{min}$.

We plan to explore the FSCF in more detail in future papers. In paper II of this series we will compute the three point correlation function for these faint sources. In paper III we will discuss the theory of gravitational lensing on the FSCF in more details and apply our results to the three environments mentioned above. In paper IV we will use existing data to attempt to observe this lensing phenomenon and examine in depth the possibility of making a more precise measurement in a larger dataset.

8 ACKNOWLEDGMENTS

We thank Phil Marshall and David Hogg for useful discussions and guidance. We thank the GOODS team, particularly Leonidas Moustakas and Victoria Laidler, for consultation on source extraction and software. This work was supported by the NSF under award AST05-07732 and in part by the U.S Department of Energy under contract number DE-AC02-76SF00515.

REFERENCES

- Alam S. M. K., Ryden B. S., 2002, *ApJ*, 570, 610
Babul A., Rees M. J., 1992, *MNRAS*, 255, 346
Beckwith S. V. W., Stiavelli M., Koekemoer A. M., Caldwell J. A. R., Ferguson H. C., Hook R., Lucas R. A., Bergeron L. E., Corbin M., Joglee S., Panagia N., Robberto M., Royle P., Somerville R. S., Sosey M., 2006, *AJ*, 132, 1729
Benford D. J., Lauer T. R., 2006, in *Space Telescopes and Instrumentation I: Optical, Infrared, and Millimeter*. Edited by Mather, John C.; MacEwen, Howard A.; de Graauw, Mattheus W. M.. *Proceedings of the SPIE*, Volume 6265, pp. 626528 (2006). Vol. 6265 of Presented at the Society of Photo-Optical Instrumentation Engineers (SPIE) Conference, *Destiny: a candidate architecture for the Joint Dark Energy Mission*
Benitez N., Ford H., Bouwens R., Menanteau F., Blakeslee J., Gronwall C., Illingworth G., Meurer G., Broadhurst T. J., Clampin M., Franx M., 2003, *ArXiv Astrophysics e-prints*
Bernstein R. A., Freedman W. L., Madore B. F., 2002, *ApJ*, 571, 107
Bertin E., Arnouts S., 1996, *A&AS*, 117, 393
Brainerd T. G., Smail I., Mould J., 1995, *MNRAS*, 275, 781
Coe D., Benítez N., Sánchez S. F., Jee M., Bouwens R., Ford H., 2006, *AJ*, 132, 926
Connolly A. J., Scranton R., Johnston D., Dodelson S., Eisenstein D. J., Frieman J. A., Gunn J. E., Hui L., Jain B., Kent S., Loveday J., Nichol R. C., O’Connell L., Postman M., 2002, *ApJ*, 579, 42
Connolly A. J., Szalay A. S., Brunner R. J., 1998, *ApJ*, 499, L125+
Frigo M., Johnson S. G., 2005, *Proceedings of the IEEE*, 93, 216
Gardner J. P., Mather J. C., Clampin M., Doyon R., Greenhouse M. A., Hammel H. B., Hutchings J. B., Jakobsen P., Lilly S. J., Long K. S., Lunine J. I., 2006, *Space Science Reviews*, 123, 485
Giavalisco M., Ferguson H. C., Koekemoer A. M., Dickinson M., Alexander D. M., Bauer F. E., Bergeron J., Biagetti C., Brandt W. N., Casertano S., Cesarsky C., Chatzichristou E., Conselice C., 2004, *ApJ*, 600, L93
Hamilton A. J. S., 1993, *ApJ*, 417, 19
Hawkins E., Maddox S., Cole S., Lahav O., Madgwick D. S., Norberg P., Peacock J. A., Baldry I. K., Baugh C. M., Bland-Hawthorn J., Bridges T., Cannon R., Colless M., Collins C., 2003, *MNRAS*, 346, 78
He P., Zou Z.-L., Zhang Y.-Z., 2000, *Ap&SS*, 274, 557
Ivezic Z., Tyson J. A., Allsman R., Andrew J., Angel R., for the LSST Collaboration 2008, *ArXiv e-prints*, 805
Jedicke R., Magnier E. A., Kaiser N., Chambers K. C., 2007, in *Valsecchi G. B., Vokrouhlický D., eds, IAU Symposium Vol. 236 of IAU Symposium, The next decade of Solar System discovery with Pan-STARRS*. pp 341–352
Jester S., Schneider D. P., Richards G. T., Green R. F., Schmidt M., Hall P. B., Strauss M. A., Berk D. E. V., Stoughton C., Gunn J. E., Brinkmann J., Kent S. M., Smith J. A., Tucker D. L., Yanny B., 2005, *Astronomical Journal*, 130, 873
Kimble R. A., MacKenty J. W., O’Connell R. W., 2006, in *Space Telescopes and Instrumentation I: Optical, Infrared, and Millimeter*. Edited by Mather, John C.; MacEwen, Howard A.; de Graauw, Mattheus W. M.. *Proceedings of the SPIE*, Volume 6265, pp. 62650I (2006). Vol. 6265 of Presented at the Society of Photo-Optical Instrumentation Engineers (SPIE) Conference, *Status and performance of HST/Wide Field Camera 3*
Krist J., 1995, in *Shaw R. A., Payne H. E., Hayes J. J. E., eds, Astronomical Data Analysis Software and Systems IV Vol. 77 of Astronomical Society of the Pacific Conference Series, Simulation of HST PSFs using Tiny Tim*. pp 349–+
Li C., Kauffmann G., Heckman T., Jing Y. P., White S. D. M., , 2007, *Interaction-induced star formation in a complete sample of 10^5 nearby star-forming galaxies*
Limber D. N., 1953, *ApJ*, 117, 134
Masjedi M., Hogg D. W., Cool R. J., Eisenstein D. J., Blanton M. R., Zehavi I., Berlind A. A., Bell E. F., Schneider D. P., Warren M. S., Brinkmann J., 2006, *ApJ*, 644, 54
Peacock J. A., Smith R. E., 2000, *MNRAS*, 318, 1144
Peebles P. J. E., 1974, *A&A*, 32, 197
Scoville N., Abraham R. G., Aussel H., Barnes J. E., Benson A., Blain A. W., Calzetti D., Comastri A., Capak P., Carilli C., Carlstrom J. E., Carollo C. M., 2007, *ApJS*, 172, 38
SNAP Collaboration 2005, *ArXiv Astrophysics e-prints*

- Tegmark M., Strauss M. A., Blanton M. R., Abazajian K., Dodelson S., Sandvik H., Wang X., Weinberg D. H., Zehavi I., Bahcall N. A., Hoyle F., Schlegel D., Scoccimarro R., Vogeley M. S., 2004, *Phys.Rev.D*, 69, 103501
- The Dark Energy Survey Collaboration 2005, ArXiv Astrophysics e-prints
- Totsuji H., Kihara T., 1969, *PASJ*, 21, 221
- Villumsen J. V., Freudling W., da Costa L. N., 1997, *ApJ*, 481, 578
- Zehavi I., Blanton M. R., Frieman J. A., Weinberg D. H., Mo H. J., Strauss M. A., Anderson S. F., Annis J., Bahcall N. A., Bernardi M., Briggs J. W., 2002, *ApJ*, 571, 172
- Zehavi I., Weinberg D. H., Zheng Z., Berlind A. A., Frieman J. A., Scoccimarro R., Sheth R. K., Blanton M. R., Tegmark M., Mo H. J., Bahcall N. A., Brinkmann J., Burles S., Csabai I., Fukugita M., 2004, *ApJ*, 608, 16